

Modal interaction in chaotic vibrations of a shallow double-curved shell-panel

S. Maruyama^a, K. Nagai^{a,*}, Y. Tsuruta^b

^a*Department of Mechanical System Engineering, Graduate School of Engineering, Gunma University,
1-5-1 Tenjin-cho, Kiryu, Gunma 376-8515, Japan*

^b*Fujitsu Ten Limited, 1-2-28 Goshō-dori, Hyogo-ku, Kobe, Hyogo 652-8510, Japan*

Accepted 20 February 2008

The peer review of this article was organised by the Guest Editor

Available online 11 April 2008

Abstract

Experimental results and analytical results are presented on chaotic vibrations of a shallow double-curved shell-panel subjected to gravity and periodic excitation. Modal interactions in the chaotic responses are discussed. The shell-panel with square boundary is simply supported for deflection. In-plane displacement at the boundary is elastically constrained. In the experiment, time histories of the chaotic responses at the spatial multiple positions of the shell-panel are measured for the inspection of modal interaction. In the analysis, the shallow shell-panel is assumed to have constant curvatures along to orthogonal directions and geometric initial imperfection. The Donnell–Mushtari–Vlasov type equation is used as governing equation with lateral inertia force. Assuming deflection with multiple modes of vibration, the governing equation is reduced to a set of nonlinear ordinary differential equations by the Bubnov–Galerkin procedure. Chaotic responses are integrated numerically. The chaotic responses, which are obtained by the experiment and the analysis, are inspected with the Fourier spectra, the Poincaré projections, the maximum Lyapunov exponents and the Lyapunov dimension. Contribution of modes of vibration to the chaotic responses is analyzed by the principal component analysis, i.e., Karhunen–Loève transformation.

© 2008 Elsevier Ltd. All rights reserved.

1. Introduction

Thin shells and plates are used as fundamental elements of light weight structures such as aircraft, spacecraft and vehicles. The shell has higher bending stiffness than that of a plate because of the curvature of the shell surface. Then, the shell can sustain larger lateral force. However, when the lateral force on the shell exceeds the critical magnitude, snap-through transition of the shell will occur owing to the buckling phenomenon. Furthermore, when the shell is subjected to periodic excitation force, nonlinear resonance responses of the shell are generated. In typical regions of the excitation frequency and of the excitation amplitude, chaotic vibrations are generated accompanied by the dynamic snap-through transition, even though the amplitude of excitation is small. Since chaotic vibrations exhibit random-like responses,

*Corresponding author. Tel.: +81 277 30 1584; fax: +81 277 30 1599.

E-mail addresses: maruyama@me.gunma-u.ac.jp (S. Maruyama), nagai@eng.gunma-u.ac.jp (K. Nagai).

higher modes of vibration as well as the fundamental mode of vibration are involved in the responses. Therefore, the chaotic vibrations of the shell may cause cyclic fatigue. The generation of the chaotic vibration is drastically influenced by small variation of shell configuration and of constraint conditions at the boundary of the shell. In practical design of shell structures, it is important to reveal the chaotic responses as well as the resonance response of the shell.

Resonance responses of shells have been studied by many researchers [1–10]. Chaotic phenomena of shell type structures were studied mainly for plates and shallow shell-panels. Chaotic responses of an infinitely long buckled plate were studied by Dowell [11]. Nayfeh and Raouf [12] studied bifurcations of nonlinear responses of an infinitely long cylindrical shell. Nonlinear periodic responses and chaotic responses of a square plate were studied by Yang and Sethna [13] and Chang et al. [14]. Chaotic responses of saddle form cable-suspended roofs and a shallow spherical shell were analyzed by Fan et al. [15] and by Soliman and Gonçalves [16], respectively. These problems were analyzed by considering a reduced number of degree-of-freedom. Amabili [17] analyzed nonlinear vibrations of doubly curved shallow shells and chaotic responses were calculated. Finite element approaches to shallow shell-panels were conducted by Zhou et al. [18] and by Sansour et al. [19]. Experiments of nonlinear responses of a panel and buckled plates under acoustic pressure were conducted by Meastrello et al. [20] and by Murphy et al. [21], respectively.

Nonlinear responses of an arch and a post-buckled beam show fundamental features of responses of a shell-panel. The authors have studied nonlinear responses of a clamped arch [22,23] and chaotic responses of a post-buckled beam [24–28] both by experiment and analysis. The predominant chaotic responses are bifurcated from the sub-harmonic resonance responses of $1/2$ and $1/3$ orders. For chaotic vibrations of shell-panels, the authors have presented the analytical results on chaotic responses of a shallow circular-cylindrical shell-panel with simply supported rectangular boundary [29], and with an in-plane elastic support at the boundary [30]. The governing equation of the shell-panel is reduced to a multiple-degree-of-freedom system. The chaotic vibrations were examined for various shell curvatures [29]. Furthermore, chaotic responses of the cylindrical shell-panel with a concentrated mass were studied [31]. Recently, experimental results associated with the analytical results on chaotic vibrations of a cylindrical shell-panel were presented by the authors [32]. Quantitative excellent agreements were obtained for the chaotic time responses, the figures of the Poincaré projections, the maximum Lyapunov exponents and the number of vibration modes which contributes to the chaos. However, vibration modes generated in the chaos cannot be confirmed by the convergence of the maximum Lyapunov exponent by increasing the embedding dimension. The principal component analysis enables an optimal estimation of linear vibration modes and contribution ratio to the chaotic responses [33].

In this paper, to investigate modal interaction in the chaotic responses of a shallow double-curved shell-panel, both experimental and analytical results are presented, including the principal component analysis. The shallow double-curved shell-panel is simply supported for deflection at a square boundary. In-plane displacements at the boundary are constrained elastically. The shell-panel is subjected to gravity and periodic lateral excitation. In the experiment, a thin shallow shell-panel is used with square form and small curvatures along the orthogonal directions in the double-curved surface. All edges of the shell-panel are supported by flexible adhesive films. Then, the above boundary conditions are satisfied. First, linear natural frequencies and characteristics of restoring force of the shell-panel are measured. Next, by exciting the shell-panel with lateral periodic acceleration, the nonlinear frequency–response curves are obtained. Chaotic time responses are detected at multiple positions of the shell-panel. In the analysis, the Donnell–Mushtari–Vlasov equation, with geometric initial imperfection and lateral inertia force is used as a governing equation. Applying the Bubnov–Galerkin procedure, the equation is reduced to a set of nonlinear ordinary differential equations. Multiple modes are taken into account in the analysis. Nonlinear periodic responses are calculated by the harmonic balance method. Time histories of the chaotic responses are calculated numerically by the Runge–Kutta–Gill method. Chaotic phenomena of the shallow shell-panel are discussed by comparing the results of the experiment and the analysis. Chaotic time responses are inspected by the Fourier spectra, the Poincaré projections, the maximum Lyapunov exponents and the Lyapunov dimension. Contribution of vibration modes to the chaotic responses is inspected by the principal component analysis.

2. Shallow shell-panel and supporting condition

For the test specimen of the shallow double-curved shell-panel, a phosphor-bronze sheet of thickness 0.198 mm is cut to square form. Both surfaces of the shell-panel are painted with acrylic resin of white color. The white surface of the shell-panel increases the measuring accuracy of the deflection as a reflection target of a laser displacement sensor used in the experiment. The thickness h of the shell-panel including the painted layer is $h = 0.24$ mm. Young's modulus E and the mass density ρ of the shell-panel are measured as $E = 62.4$ GPa and $\rho = 7.52 \times 10^3$ kg/m³, respectively, including the painted layer. Poisson's ratio ν is taken as 0.33. Fig. 1 shows the shallow shell-panel and a rectangular supporting frame. The supporting frame made of duralumin has square form with inner length 140 mm. Side lengths of the shell-panel are measured as $a = 139.7$ mm and $b = 139.5$ mm. All edges of the shell-panel are supported by the frame through the strips of flexible adhesive film. The thickness of the film is 0.072 mm. One end of the adhesive film wraps around the edge of the shell-panel, while the other end is glued to the inner wall of the frame. As shown in the figure, the strips of films are glued alternately along the panel edge, then the boundary of the shell satisfies the conditions of simply support for deflection and of elastic constraint for in-plane displacement. In the figure, the x -axis and the y -axis are defined along the edges of the double-curved shell-panel and the z -axis is defined perpendicular to the shell surface. In-plane displacements U and V are denoted along the x -axis and the y -axis, respectively. The deflection of the shell-panel is denoted by W along the z -axis. The shell-panel is subjected to the gravitational acceleration g and periodic acceleration $a_d \cos \Omega t$ in the lateral direction of the shell surface, where a_d , Ω and t correspond to the amplitude of excitation, the excitation angular frequency and time, respectively. The periodic acceleration to the shell-panel is applied by shaking the supporting frame with an electromagnetic exciter.

In the experiment, initial curved configuration of the shell surface is measured by the laser displacement sensor. To minimize the static lateral deformation of the shell-panel by the gravitational force, the initial configuration is measured by setting the shell surface parallel to the gravitational direction. The configuration of the shell-panel is shown in Fig. 2. In the figure, the shell-panel has the curved configuration both in the x -direction and in the y -direction. The radii of curvature r_x and r_y are denoted in the x -direction and in the y -direction, respectively. The radii of curvature are approximated by the least square method in each direction.

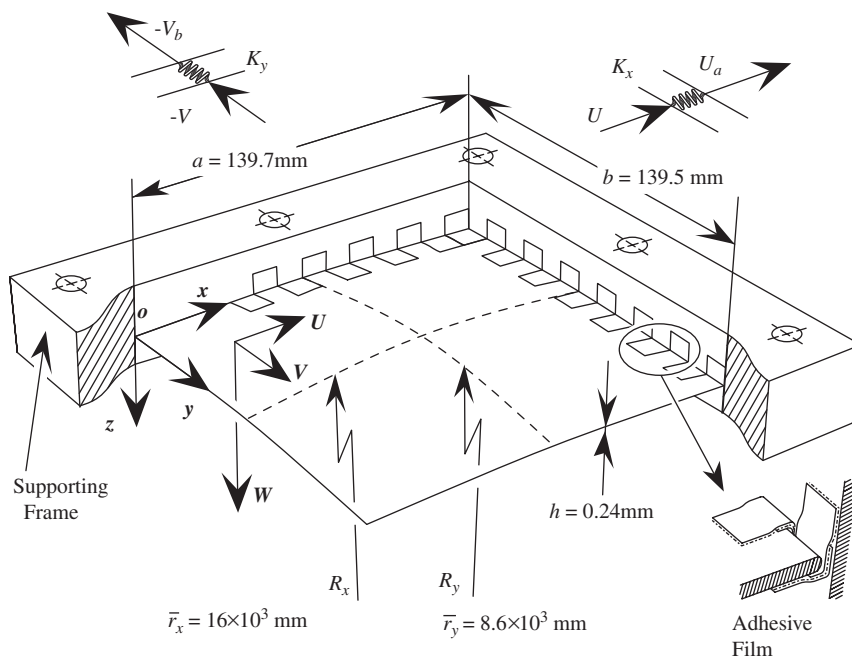


Fig. 1. Shallow double-curved shell-panel and supporting condition.

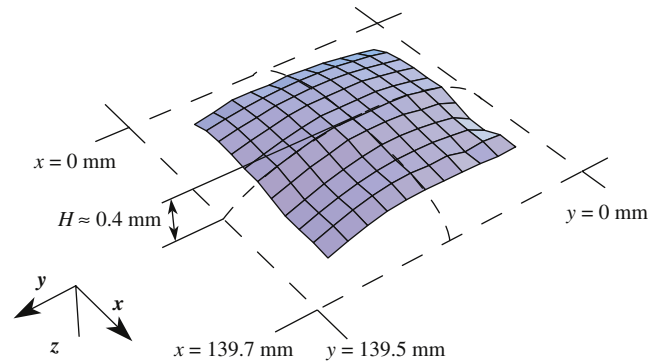


Fig. 2. The configuration of the shell-panel parallel to the gravity.

At the typical positions y/b , the radii r_x along the x -direction are shown as follows:

$$(y/b = 0.21, r_x = 11 \times 10^3 \text{ mm}), \quad (0.5, 9.3 \times 10^3 \text{ mm}), \quad (0.79, 20 \times 10^3 \text{ mm}).$$

In the y -direction, the radii r_y are obtained as

$$(x/a = 0.21, r_y = 12 \times 10^3 \text{ mm}), \quad (0.5, 7.2 \times 10^3 \text{ mm}), \quad (0.79, 8.1 \times 10^3 \text{ mm}).$$

It is found that the radii of curvature at the center of the shell-panel are smaller than the radii near the boundaries. Averaged radii \bar{r}_x and \bar{r}_y including the radii at other positions are calculated as: $\bar{r}_x = 16 \times 10^3 \text{ mm}$, $\bar{r}_y = 8.6 \times 10^3 \text{ mm}$. In the figure, symmetric and asymmetric geometric imperfection remains in the configuration of the shell-panel measured from the curved surface with the averaged radii \bar{r}_x and \bar{r}_y . Then the total configuration of the shell-panel can be expressed as a double-curved surface including the symmetric and asymmetric initial imperfection. The boundary of the shell-panel has small undulation along the edges less than 0.14 mm.

For the analysis, the shell-panel is assumed to have a shallow double-curved configuration with radii of curvature R_x and R_y along the x -direction and the y -direction, respectively, and geometric imperfection. The shell-panel is assumed to be simply supported for deflection along all edges of the rectangular boundary. Furthermore, for the in-plane displacement, the opposite edges are assumed to be attached to in-plane springs with equal stiffness. The springs act only in normal directions to the edges. At the edges $x = 0$ and $x = a$, the spring constant per unit length is denoted by K_x , while the in-plane springs at the edges $y = 0$ and $y = b$ have the spring constant K_y .

3. Procedure of experiments

The shell-panel is initially deformed by the gravitational force to the static deflection. The shell-panel and the supporting frame are excited laterally by the electromagnetic exciter. Dynamic responses of the shell-panel relative to the supporting frame are detected by the laser displacement meter.

3.1. Measurement of linear natural frequencies and nonlinear restoring force

As fundamental properties of the shell-panel, linear natural frequencies and characteristics of nonlinear restoring force are measured.

Applying periodic sound pressure on the shell-panel, resonant response with infinitesimal small amplitude is measured by the laser displacement sensor. Natural frequencies of the shell-panel are inspected with a spectrum analyzer. Natural modes of vibration are detected by scanning the sensor over the shell surface. Characteristics of nonlinear restoring force of the shell-panel are obtained through the static deflection by static concentrated force. The laser displacement sensor and a load cell are used. The concentrated force is applied to the shell-panel, by pressing the detection-needle of the load cell to the shell-panel. Then, the

shell-panel deflects to an equilibrium position. Thus, the characteristics of the nonlinear restoring force of the shell-panel can be obtained.

3.2. Procedure of vibration test on chaotic responses

Fig. 3 shows a schematic diagram of a vibration test apparatus. The supporting frame of the shell-panel, which is mounted on the vibration table, is shaken periodically with an electromagnetic exciter. Thus, periodic lateral acceleration can be applied on the shell-panel. The excitation is provided by the devices as numbered from 1 to 5. The exciter controller 1 generates a sinusoidal periodic signal. The periodic signal is amplified through the power amplifier 2. The vibration exciter 3 drives the supporting frame with periodic acceleration. The accelerometer pickup 4 fixed on the frame detects the acceleration applied on the shell-panel 5. The signal of acceleration is fed back to the controller 1. Thus, the peak amplitude of acceleration can be fixed to a constant level during a sweep of the excitation frequency. Dynamical responses of the shell-panel are measured with the instruments of the multiple laser displacement sensor from 6 to 8. To inspect modal patterns generated in the chaotic responses, six sets of laser displacement sensors 6 are arranged over the shell surface. The displacement of the shell-panel relative to the supporting frame is detected with the laser displacement sensors 6 and the sensor 7. One of the sensors 6 measures the responses of the shell-panel and the periodic displacement of the frame simultaneously. The sensor 7 measures the periodic displacement of the frame only. The controller 8 subtracts the two signals. With this subtraction, the pure dynamic response $w(\tau)$ of the shell-panel can be detected, where w and τ indicate the non-dimensional deflection and time, respectively, which will be defined in Section 4. One of the sensors 6 is set on the sliding table 9 and the sensor travels on the surface of the shell-panel. Thus, static deflection and the vibration mode can be inspected.

Nonlinear frequency–response curves of the shell-panel are obtained by sweeping the excitation frequency. The time responses of the shell-panel detected by the laser sensors are transformed to the amplitude in a root mean square value w_{rms} with the digital voltmeter 10. The excitation frequency applied on the shell-panel is counted with the digital frequency counter 11 through the signal of periodic acceleration measured with the accelerometer 4. The amplitude w_{rms} of the shell response and the excitation frequency f are transferred to the computer 12. In the figure, ω denotes the non-dimensional excitation frequency which is defined in Section 4.

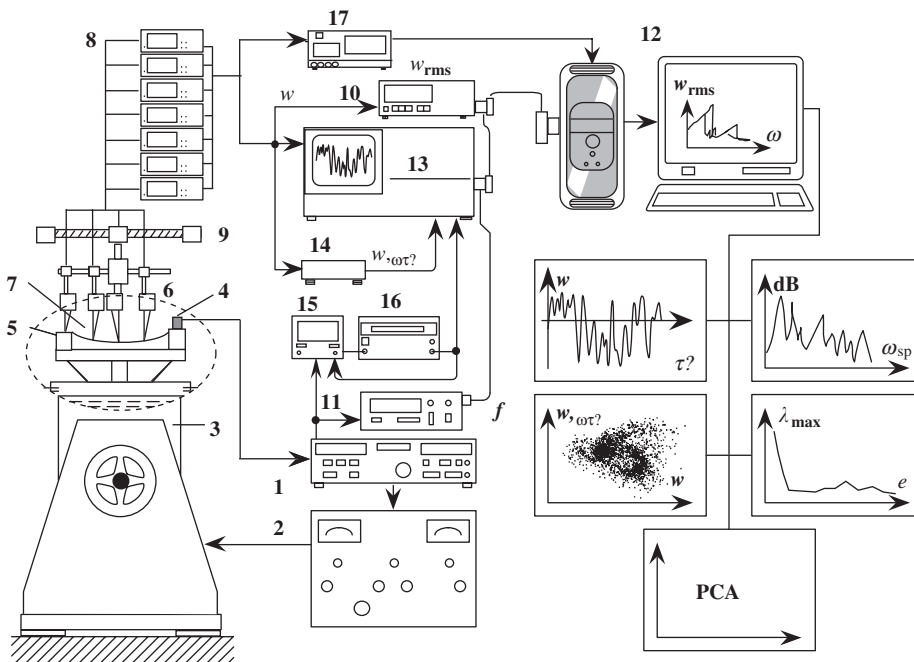


Fig. 3. Vibration test apparatus.

Then, the nonlinear frequency–response curves are recorded with the relation between w_{rms} and ω . The digital spectrum analyzer 13 records time responses of chaotic vibrations and transforms the responses to the Fourier spectra. Furthermore, the chaotic time responses are transmitted to the computer 12 and the maximum Lyapunov exponents λ_{max} are calculated. The Poincaré projection of the response is obtained by the following step. Dynamic displacement of the chaotic responses is transformed to velocity by the differentiation amplifier 14. The set of the displacement w and the velocity $w_{,\omega\tau}$ is sampled sequentially based on a sampling pulse once in every period of the excitation. The pulse is generated with the phase meter 15 and the delayed pulse oscillator 16. The Poincaré projections of the chaotic response are stored in the computer 12. To inspect contributions of multiple vibration modes to the chaotic responses, time responses at six positions over the shell-panel are recorded with the multi-channel digital recorder 17.

In the vibration test, the chaotic response of the shell-panel is drastically influenced by a small deviation of thermal elongation. To obtain precise results of the chaotic responses, the in-plane thermal elongation of the shell-panel relative to the supporting frame should be kept constant during the vibration test. The temperatures both of the shell-panel and the supporting frame are kept constant within 20 ± 0.5 degree of centigrade [32].

4. Procedure of analysis

4.1. Governing equations and boundary conditions

The geometry of the shallow double-curved shell-panel and the supporting conditions are explained in Section 2. In the experiment, the chaotic response of the thin shell-panel is restricted to lower frequency range where bending vibrations are dominant, then the effects of in-plane inertia forces can be neglected in the analysis. The magnitude of the in-plane inertia is estimated to be less than 10^{-3} times of the terms of in-plane stress resultants in the in-plane equation of motion. The Donnell–Mushtari–Vlasov type equations [34] modified with lateral inertia force are employed.

Denoting the total deflection and the geometric initial imperfection by W and W_0 , respectively, and the stress function by F , the non-dimensional governing equations of the shell-panel, including lateral inertia force are shown as

$$\nabla^4 f = c[\beta^2(w_{,\xi\xi\eta}^2 - w_{0,\xi\xi\eta}^2 - w_{,\xi\xi}w_{,\eta\eta} + w_{0,\xi\xi}w_{0,\eta\eta}) - \alpha_x\beta^2(w - w_0)_{,\eta\eta} - \alpha_y(w - w_0)_{,\xi\xi}], \quad (1)$$

$$L(w, w_0, f) \equiv w_{,\tau\tau} + \nabla^4(w - w_0) - \alpha_x\beta^2 f_{,\eta\eta} - \alpha_y f_{,\xi\xi} - \beta^2(f_{,\xi\xi}w_{,\eta\eta} - 2f_{,\xi\eta}w_{,\xi\eta} + f_{,\eta\eta}w_{,\xi\xi}) - (p_s + p_d \cos \omega\tau) - q_s \delta(\xi - \xi_1) \delta(\eta - \eta_1) = 0, \quad (2)$$

where $\nabla^2 \equiv \partial^2/\partial\xi^2 + \beta^2\partial^2/\partial\eta^2$ is the Laplace operator. Eq. (1) corresponds to the compatibility equation in terms of the stress function of the shell-panel, while Eq. (2) shows the equation of motion for the deflection coupled with the stress function. The following non-dimensional quantities are introduced.

$$\begin{aligned} [\xi, \xi_1] &= [x, x_1]/a, & [\eta, \eta_1] &= [y, y_1]/b, & \beta &= a/b, & \alpha_x &= a^2/R_x h, & \alpha_y &= a^2/R_y h, \\ [w, w_0] &= [W, W_0]/h, & [u, v] &= [U, V](a/h^2), \\ [n_x, n_y, n_{xy}] &= [N_x, N_y, N_{xy}](a^2/D), & f &= F/D, & [k_x, k_y] &= [K_x, K_y](ah^2/D), \\ [p_s, p_d] &= [g, a_d](\rho a^4/D), & q_s &= Q_s a^2 \beta / Dh, & \tau &= \Omega_0 t, & \omega &= \Omega / \Omega_0. \end{aligned} \quad (3)$$

In the foregoing, $\Omega_0 = (1/a^2)\sqrt{D/\rho h}$ and $c = 12(1 - \nu^2)$ are used, where $D = Eh^3/12(1 - \nu^2)$ is the bending stiffness of the shell-panel, E , ν and ρ are Young's modulus, Poisson's ratio and the mass density of the shell-panel, respectively. The value of h , E and ρ are measured including the painted layer. The symbols ξ and η are the non-dimensional coordinates. The symbol β is the aspect ratio of the rectangular boundary of the shell-panel. The symbols α_x and α_y are the non-dimensional shell curvatures in the x -direction and the y -direction, respectively. The symbols w and w_0 are the non-dimensional deflections, while u and v are the in-plane displacements in the ξ -direction and the η -direction, respectively. In Eqs. (1) and (2), subscripts following a comma denote partial differentiations. The symbols N_x , N_y and N_{xy} are the stress resultants acting

on a cross-section perpendicular to the x -direction and the y -direction. The symbols k_x and k_y represent the non-dimensional coefficients of the in-plane springs attached to the edges ($\xi = 0$ and 1) and the edges ($\eta = 0$ and 1), respectively. The symbols p_s and p_d correspond to the non-dimensional intensity of distributed force by the gravitational acceleration g and the periodic acceleration a_d , respectively. The symbol q_s is the non-dimensional concentrated force. To measure the characteristics of the nonlinear restoring force of the shell-panel, a concentrated force Q_s is loaded at the point ($x = x_1, y = y_1$). The symbols ω and τ are the non-dimensional excitation frequency and the non-dimensional time, respectively. The non-dimensional stress resultants n_x, n_y and n_{xy} are related to the stress function f as

$$n_x = \beta^2 f_{,\eta\eta}, \quad n_y = f_{,\xi\xi}, \quad n_{xy} = -\beta f_{,\xi\eta}. \tag{4}$$

The in-plane displacements u and v are related to w, w_0 and f as

$$\begin{aligned} c[u_{,\xi\xi} - \alpha_x w + (1/2)w_{,\xi\xi}^2] &= \beta^2 f_{,\eta\eta} - v f_{,\xi\xi}, \\ c[\beta v_{,\eta} - \alpha_y w + (\beta^2/2)w_{,\eta}^2] &= f_{,\xi\xi} - v\beta^2 f_{,\eta\eta}, \\ c[\beta u_{,\eta} + v_{,\xi} + \beta w_{,\xi} w_{,\eta}] &= -2\beta(1 + \nu) f_{,\xi\eta}. \end{aligned} \tag{5}$$

The simply supported conditions for the deflection along all edges of the shell-panel is shown as

$$\xi = 0, 1 : w = 0, w_{,\xi\xi} = 0, \quad \eta = 0, 1 : w = 0, w_{,\eta\eta} = 0. \tag{6}$$

The in-plane boundary conditions are assumed as

$$\begin{aligned} \xi = 0 : \int_0^1 [n_x - k_x(u - u_0)] d\eta &= 0, \quad \int_0^1 n_{xy} d\eta = 0, \\ \xi = 1 : \int_0^1 [n_x + k_x(u - u_a)] d\eta &= 0, \quad \int_0^1 n_{xy} d\eta = 0, \\ \eta = 0 : \beta \int_0^1 [n_y - k_y(v - v_0)] d\xi &= 0, \quad \beta \int_0^1 n_{xy} d\xi = 0, \\ \eta = 1 : \beta \int_0^1 [n_y + k_y(v - v_b)] d\xi &= 0, \quad \beta \int_0^1 n_{xy} d\xi = 0. \end{aligned} \tag{7}$$

In the foregoing, u_0, u_a, v_0 and v_b are the initial in-plane displacements for the outer part of the in-plane springs connected to the edges of the shell-panel. The in-plane stress resultant and the restoring force of the in-plane spring are in equilibrium with averaged form along the edges [35]. The problem consists of finding the solutions w and f which satisfy the governing equations and the boundary conditions.

4.2. Reduction to multiple-degree-of-freedom system

Using the Bubnov–Galerkin method, the governing equations of the shallow double-curved shell-panel with geometric initial imperfection is discretized to the equations of a multiple-degree-of-freedom system. The same procedure was applied to the problems of a shallow cylindrical shell-panel [30–32] by the authors. In this paper, the procedure is summarized briefly. The deflections w and w_0 of the shell-panel are assumed as

$$\begin{aligned} [w(\xi, \eta, \tau), w_0(\xi, \eta)] &= \sum_m \sum_n [\hat{b}_{mn}(\tau), \hat{a}_{mn}] \hat{\zeta}_{mn}(\xi, \eta), \quad (m, n = 1, 2, 3, \dots), \\ \hat{\zeta}_{mn}(\xi, \eta) &= \sin m\pi\xi \sin n\pi\eta, \end{aligned} \tag{8}$$

where \hat{b}_{mn} is an unknown time function and \hat{a}_{mn} is the given constant representing the geometric initial imperfection, while $\hat{\zeta}_{mn}$ is the coordinate function. The indices m and n denote the half-wave numbers of the coordinate function along the x -axis and the y -axis, respectively. The stress function f can be expressed by the homogeneous solution and particular solution, in terms of the unknown function \hat{b}_{mn} , of the compatibility equation (1), as shown in the appendix. The Galerkin procedure is applied to the equation of motion (2),

the following condition is derived for the coordinate function $\hat{\zeta}_{rs}$ as:

$$\int_0^1 \int_0^1 L(w, w_0, f) \hat{\zeta}_{rs}(\xi, \eta) d\xi d\eta = 0, \quad (r, s = 1, 2, 3, \dots). \tag{9}$$

Substituting both Eqs. (8) and the solution of f into Eq. (9) and performing the integration, the set of nonlinear ordinary differential equations, in terms of $\hat{b}_{mn}(\tau)$, is reduced. In Eq. (9), the subscripts r and s of the coordinate function $\hat{\zeta}_{rs}$ imply the half-wave numbers of the configuration of deflection in the ξ -direction and the η -direction, respectively. A combination of the subscripts r and s represents the modal pattern of deflection, which can be referred as a new index i . The unknown time function $\hat{b}_{mn}(\tau)$ is replaced by a new variable $\check{b}_j(\tau)$, i.e., $\check{b}_j \equiv \hat{b}_{mn}$, $\check{\zeta}_j \equiv \hat{\zeta}_{mn}$. These variables are counted in the order of a set of the half-wave numbers of the shell configuration. For example, \hat{b}_{11} , \hat{b}_{12} and \hat{b}_{21} are referred as \check{b}_1 , \check{b}_2 and \check{b}_3 , respectively. The set of nonlinear ordinary differential equations can be rearranged as follows:

$$\sum_j \check{B}_{ij} \check{b}_{j,\tau\tau} + \sum_j \check{C}_{ij} \check{b}_j + \sum_j \sum_k \check{D}_{ijk} \check{b}_j \check{b}_k + \sum_j \sum_k \sum_l \check{E}_{ijkl} \check{b}_j \check{b}_k \check{b}_l - \check{F}_i - (p_s + p_d \cos \omega\tau) \check{G}_i = 0, \quad (i, j, k, l = 1, 2, 3, \dots). \tag{10}$$

In the foregoing, \check{B}_{ij} is the coefficient of the inertia term, while the coefficients \check{C}_{ij} , \check{D}_{ijk} and \check{E}_{ijkl} correspond to the restoring forces of linear, quadratic and cubic terms, respectively. The \check{F}_i is the constant coefficient and \check{G}_i is related to the term of periodic excitation. These coefficients include the parameters of the shell geometry and the in-plane spring.

The static deformation appears under the static forces p_s and depends on the in-plane constraint at the boundary. Hence, the static deformation and the dynamic responses are solved by the following sequential procedure. First, the deflection $w(\xi, \eta, \tau)$ of the shell-panel is divided into the static deflection $\bar{w}(\xi, \eta)$ and to the dynamic displacement $\tilde{w}(\xi, \eta, \tau)$ as

$$w(\xi, \eta, \tau) = \bar{w}(\xi, \eta) + \tilde{w}(\xi, \eta, \tau), \tag{11}$$

$$[w(\xi, \eta, \tau), \bar{w}(\xi, \eta), \tilde{w}(\xi, \eta, \tau)] = \sum_j [\check{b}_j(\tau), \bar{b}_j, \tilde{b}_j(\tau)] \check{\zeta}_j(\xi, \eta), \quad (j = 1, 2, 3, \dots),$$

where \bar{b}_j is an unknown constant and $\tilde{b}_j(\tau)$ represents an unknown time function of the dynamic displacement measured from the static equilibrium position. The variable $\check{b}_j(\tau)$ is expressed as $\check{b}_j(\tau) = \bar{b}_j + \tilde{b}_j(\tau)$. Then, substituting this relation into Eq. (10), the two sets of coupled equations, with \bar{b}_j and $\tilde{b}_j(\tau)$, are obtained. From the set of cubic equations in terms of \bar{b}_j , the static deflection $\bar{w}(\xi, \eta)$ can be obtained. Thus, the equation of motion in terms of the \tilde{b}_j can measure the response from the static equilibrium position.

Furthermore, omitting the nonlinear terms as well as the terms of external periodic force, the linear equation is obtained for free vibration. The linear natural frequencies ω_i and corresponding linear natural mode of vibration $\check{\zeta}_i$ are obtained. Using the normal coordinates b_i corresponding to $\check{\zeta}_i$, the deflection \tilde{w} measured from the static equilibrium point can be expressed as

$$\tilde{w}(\xi, \eta, \tau) = \sum_i b_i(\tau) \check{\zeta}_i(\xi, \eta), \quad (i = 1, 2, 3, \dots). \tag{12}$$

Transforming the coordinate \check{b}_j to the normal coordinate b_i , one can obtain a set of nonlinear differential equations in the standard form:

$$M(b_i) \equiv b_{i,\tau\tau} + 2\varepsilon_i \omega_i b_{i,\tau} + \omega_i^2 b_i + \sum_j \sum_k D_{ijk} b_j b_k + \sum_j \sum_k \sum_l E_{ijkl} b_j b_k b_l - p_d G_i \cos \omega\tau = 0, \quad (i, j, k, l = 1, 2, 3, \dots). \tag{13}$$

The foregoing equation has couplings only in the quadratic and cubic nonlinear terms. A linear damping term is introduced, where ε_i represents a damping ratio corresponding to the i th linear mode of vibration.

4.3. Determination of periodic responses and chaotic responses

The periodic responses are calculated by the harmonic balance method [36]. The periodic solution b_i is assumed as

$$b_i = C_{i1\mu 0} + \sum_p [C_{i1\mu p} \cos \mu p \omega \tau + C_{i2\mu p} \sin \mu p \omega \tau], \quad (i = 1, 2, 3, \dots, I_c, p = 1, 2, 3, \dots), \quad (14)$$

where $C_{i1\mu 0}$, $C_{i1\mu p}$ and $C_{i2\mu p}$ are unknown constants. To obtain the solutions of principal resonance and super-harmonic resonance, μ is chosen as unity, while to get sub-harmonic resonance responses of 1/2 or 1/3 orders, μ is taken as 1/2 or 1/3, respectively.

Chaotic vibrations show random-like non-periodic responses. Therefore, to determine chaotic responses, it is required to integrate numerically the nonlinear ordinary differential equation (13). The chaotic responses of Eq. (13) is calculated numerically with the Runge–Kutta–Gill method.

4.4. Evaluation of chaotic responses

Multiple methodologies of inspection are required to confirm the chaotic responses of the shell-panel. A Fourier spectrum of a non-periodic time response shows a broadband spectrum. However, dominant components of the spectrum are related to the periodic resonance response from which the chaotic response is bifurcated. The Poincaré projections of the chaotic responses show a fractal pattern on the phase plane.

The chaotic responses can be confirmed with the Lyapunov exponent. It is defined as the exponential growth rate of the distance between two neighboring trajectories in the phase space of dynamical system. If the Lyapunov exponents have one or more positive values, the response can be confirmed as chaos. The Lyapunov exponents are calculated with the procedure proposed by Wolf et al. [37] and Takens [38]. The Lyapunov dimension d_L , which shows a fractal feature of chaos, can also be calculated by the Lyapunov exponents [39]. Furthermore, number of predominant vibration modes, which contributes to the chaos, can be estimated by the convergence of the Lyapunov dimension or the maximum Lyapunov exponent when the assumed dimension of the phase space is increased [40].

Finally, the principal component analysis [33,41], which is also called as the Karhunen–Loève transformation or the proper orthogonal decomposition, is applied. The principal component analysis enables the estimation of the modal pattern in the chaotic response. In the principal component analysis, the covariance matrix of the simultaneous time responses at multiple positions (ξ_p, η_p) , ($p = 1, 2, \dots, d$) of the shell-panel is calculated. The covariance matrix is transformed to an orthogonal matrix, which results in the eigenvalue problem of the covariance matrix. The eigenvector Φ_i ($i = 1, 2, \dots, d$) represents the modal pattern and the corresponding eigenvalue p_i denotes the contribution of the modal pattern to the chaotic response. Contribution ratio μ_i of the i th modal pattern to the all modal patterns is calculated as

$$\mu_i = p_i / \sum_{j=1}^d p_j. \quad (15)$$

The modal patterns and their contribution ratio reveal modal interaction, i.e., contribution of individual modes to the chaotic vibrations of the shell-panel.

5. Results and discussion

5.1. Fundamental properties of the shell-panel

Nonlinear and chaotic responses of the shallow shell-panel are influenced severely by the geometric initial imperfection, the shell curvature and the in-plane boundary condition. Then, the unknown parameters of the shell-panel, i.e., the geometric initial imperfection, the curvature and the stiffness of the in-plane spring, are identified with the trial-and-error computation comparing with the experimental results of the configuration of the shell surface, the linear natural frequencies and the characteristics of restoring force.

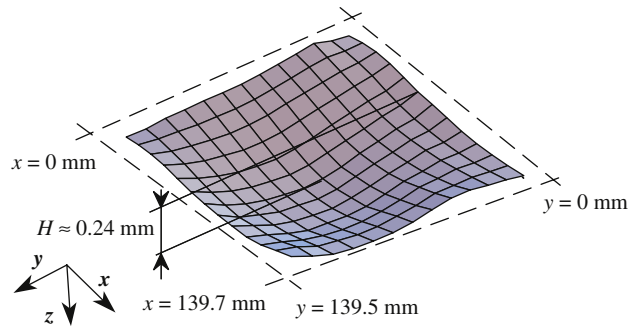


Fig. 4. The deformed configuration of the shell-panel under the gravity.

Table 1
Natural frequencies and vibration modes of the shell-panel

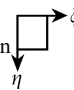






Mode	Modal pattern 	Experimental results, ω_{mn}	Analytical results, ω_{mn}	Deviation (%)
i	(m, n)			
1	(1,1) 	25.0	25.4	2
2	(2,1) 	51.1	55.4	8
3	(1,2) 	57.2	61.5	7
4	(2,2) 	86.3	67.2	28
5	(3,1) 	105	98.2	7
6	(1,3) 	112	106	6

Fig. 4 shows the deformed configuration of the shell-panel under the gravitational force $p_s = 380$. The shell-panel has large deflection due to the gravitational force which exceeds the snap-through load. Assuming the shell-panel has the double-curved configuration and the geometric initial imperfection, the following parameters have been identified.

$$\begin{aligned} \alpha_x = 4.0, \quad \alpha_y = 7.5, \quad \hat{a}_{11} = -0.4, \quad \hat{a}_{21} = -0.04, \quad \hat{a}_{12} = 0.12, \\ k_x = 0.001, \quad k_y = 0.001, \quad u_0 = u_a = 0, \quad v_0 = v_b = 0, \end{aligned} \tag{16}$$

where u_0, u_a, v_0 and v_b are the initial in-plane displacements of the outer part of the in-plane springs. Since the components $\hat{a}_{11}, \hat{a}_{21}$ and \hat{a}_{12} play the most important role for the linear natural frequencies and the characteristics of nonlinear restoring force, the other components are identified as zero. To determine the linear natural frequencies and the static deflection of the shell-panel, 16 terms are assumed for the modal expansion in Eq. (8), where integers m and n are $m, n = 1, 2, 3, 4$.

Table 1 shows the linear natural frequencies. In the table ω_{mn} stands for the non-dimensional frequency. The integers m and n denote half-wave numbers of vibration-mode along the ξ -axis and the η -axis, respectively. Modal patterns related to the natural modes of vibration are shown with the notation (m, n) . The analytical linear natural frequencies ω_{mn} are also listed in the table. The linear natural frequencies ω_{mn} of the modes (1,1), (2,1) and (1,2) obtained by the experiment are well simulated by the analytical results within the discrepancy of 5.7 percent on average. The discrepancy between the experimental results and the analytical results of the natural frequency of the mode (2,2) is larger than those of the other lower vibration modes.

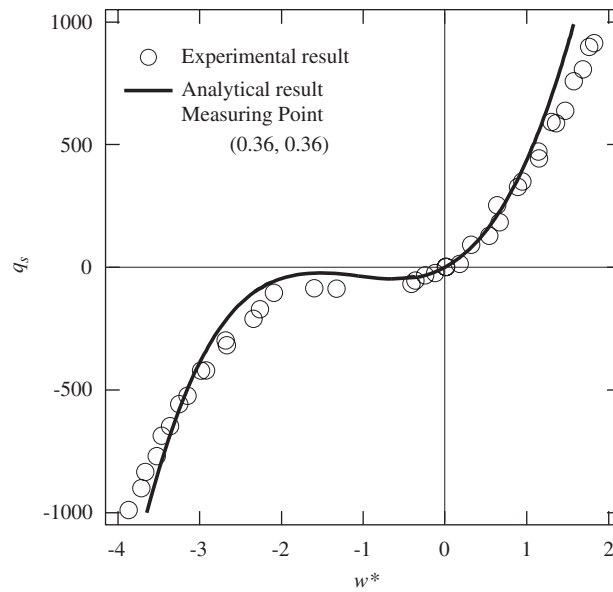


Fig. 5. Static deflection of the shell-panel by a concentrated load.

The discrepancy seems to be caused by the initial distortion of the shell-panel with higher asymmetric configuration including the undulation along the panel edges.

Fig. 5 shows the characteristics of nonlinear restoring force. The static deflections $w^*(\xi, \eta)$ of the shell-panel is shown by the concentrated force q_s acting on the center of the shell-panel. The deflections are measured from the static equilibrium positions of the shell surface under the gravitational force. The deflections w^* at the point $\xi = 0.36, \eta = 0.36$ is marked by circle.

Analytical result of the restoring force at the same point is denoted by the solid line. When the deflection of the shell-panel is increased to the negative z -direction from the static equilibrium position by the concentrated force, the gradient of curve of the restoring force decreases. Thus the characteristics of a softening spring appear. Furthermore, the gradient of curve changes from zero to negative. In the range of deflection from $w = -0.5$ to -1.8 , the curve of the restoring force shows a negative gradient. As the deflection increases larger, the restoring force exhibits the type of a hardening spring.

The characteristics of restoring force in the experiment agree fairly well with the analytical results within relatively small deflection.

5.2. Frequency–response curves of the shell-panel

To inspect the generation of chaotic responses bifurcated from resonance responses, nonlinear frequency–response curves of the shell-panel are obtained under the gravitational force $p_s = 380$ and the periodic excitation force $p_d \cos \omega\tau$. The amplitude of excitation p_d is kept constant $p_d = 760$. Experimental and analytical nonlinear frequency–response curves are shown in Figs. 6(a) and (b), respectively. In the figure, the abscissa indicates the excitation frequency ω which covers the range from $\omega = 20$ to 80 . Natural frequencies of the shell-panel are also indicated by the white circles on the abscissa. The ordinate shows the non-dimensional amplitude \tilde{w}_{rms} of the responses with a root mean square value of the deflection \tilde{w} at the position $\xi = 0.79$ and $\eta = 0.21$. The frequency of the excitation is swept very slowly to avoid transient effects on the chaotic response of the shell-panel in the experiment. The amplitude \tilde{w}_{rms} is averaged with relatively long time interval. In the experimental result shown in Fig. 6(a), the solid line indicates the frequency–response curve, while the dotted lines show the frequencies where jump phenomena occur. In typical frequency ranges, non-periodic response is generated with amplitude modulation of \tilde{w}_{rms} . In the analytical result shown in Fig. 6(b), the thick solid lines indicate the frequency–response curves of the stable periodic responses obtained by the harmonic balance method. For the computation of nonlinear dynamical responses, first six modes are considered within

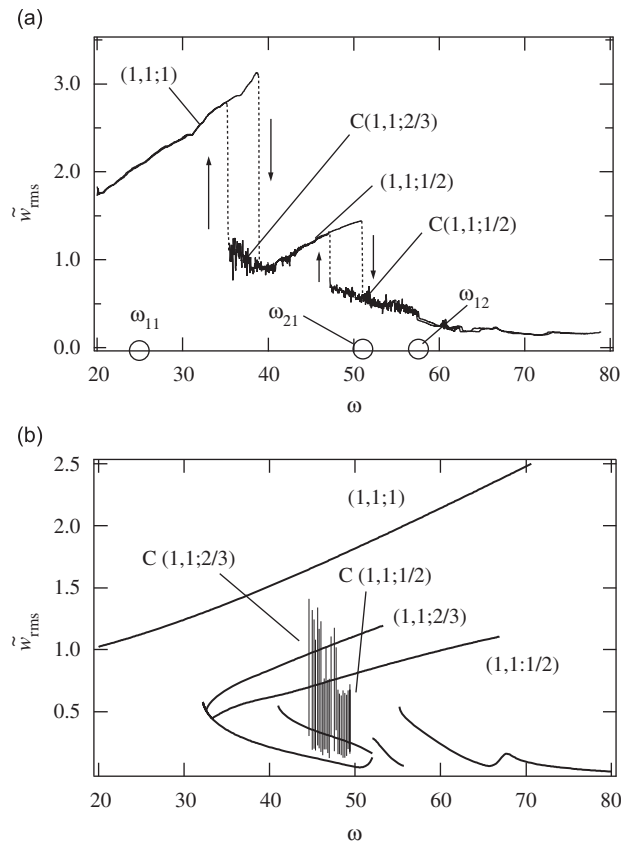


Fig. 6. Frequency–response curve of the shell-panel ($p_d = 776$, measured at $\xi = 0.79, \eta = 0.21$): (a) experimental results; (b) analytical results.

relatively lower excitation frequency range. The linear damping ratios of the individual modes are assumed as $\varepsilon_i = 0.014$ ($i = 1, 2, \dots, 6$). The damping ratio is estimated for the lowest vibration mode from experimental results of damped free vibration of the shell-panel and is assumed to be the same for all the vibration modes. The non-stationary amplitudes of the chaotic responses are indicated with thin solid lines. The chaotic responses are calculated by the numerical integration. The amplitudes of the chaotic response are averaged within short time intervals. Comparing the frequency–response curves of the experiment with the analytical ones, the type of the periodic resonance is determined by the notation $(m, n : j)$. Former indices m and n indicate the mode of vibration generated in the resonance, while index j stands for the order of the periodic resonance. For example, $(1,1;1)$ indicates the response of the principal resonance corresponding to the lowest mode of vibration $(1, 1)$, while $(1,1;1/2)$ means the sub-harmonic resonance of $1/2$ order.

In the experiment, as shown in Fig. 6(a), when the excitation frequency is decreased from $\omega = 80$, the non-resonant response prevails. Close to the frequency $\omega = 60$, the steady-state periodic response of the sub-harmonic resonance $(1,1;1/2)$ is generated. When the frequency is $\omega = 57$, the non-periodic response is generated. The chaotic response is bifurcated from the sub-harmonic resonance $(1,1;1/2)$ and is confirmed as the chaos by the evaluation explained later in Sections 5.3 and 5.4. The chaotic response is denoted by the notation $C(m, n : j)$, where $(m, n : j)$ represents the dominant mode of vibration and the predominant type of resonance excited in the chaotic vibration. The chaotic response $C(1, 1 : 1/2)$ covers the frequency from $\omega = 57$ to 46. The frequency–response curve of the sub-harmonic resonance of the lowest mode of vibration exhibits the nonlinear characteristics of a softening-and-hardening spring. Moreover, a new type of chaotic response $C(1, 1 : 2/3)$ is bifurcated from the sub-harmonic resonance response $(1,1;1/2)$ at the frequency $\omega = 41$. This chaotic response corresponds to the ultra-sub-harmonic resonance response $(1,1;2/3)$ and

continues within the frequency from $\omega = 41$ to 35. Finally, the chaotic response transits to the large amplitude periodic vibration of the principal resonance (1,1:1) through the jump phenomenon.

In the analytical result shown in Fig. 6(b), the chaotic responses C(1,1 : 1/2) are generated within the frequency range from $\omega = 48.0$ to 49.4. Furthermore, the other chaotic responses C(1,1 : 2/3) are also generated with lower frequency range from $\omega = 44.6$ to 47.8. The non-stationary amplitudes of the chaotic response C(1,1 : 2/3) overlap on the response curves of the sub-harmonic resonance (1,1:1/2) and the ultra-sub-harmonic resonance (1,1:2/3).

5.3. Time histories, frequency spectra and Poincaré projections of chaotic responses

Under the excitation amplitude $p_d = 776$, time histories, corresponding Fourier spectra and Poincaré projections in the region of the chaotic response C(1,1 : 1/2) are inspected in the experiment and in the analysis. At the position $\xi = 0.79$ and $\eta = 0.21$, the responses are recorded. Typical response of the experiment is shown in Fig. 7 at $\omega = 49.8$. In Fig. 7(a), the time history of the deflection \tilde{w} is shown with the time τ/τ_e normalized by the excitation period $\tau_e = 2\pi/\omega$. In the figure, the irregular movement of the chaotic response occurs especially in the negative z -direction. These response involves the dynamic snap-through transition of the shell-panel. Fig. 7(b) shows the Fourier spectrum of the chaotic responses. The ordinate indicates the amplitude A of the spectrum scaled by decibel, while the abscissa denotes the non-dimensional Fourier frequency ω_{sp} . The Fourier spectrum has predominant spike of spectrum at the half of excitation frequency $\omega/2$. The peak spike of $(2/5)\omega$ also appears in the response, within the long duration. Therefore, the chaotic response C(1,1 : 1/2) is induced dominantly from the sub-harmonic response of 1/2 order involving the harmonic component of $(2/5)\omega$ of the excitation frequency [32]. Fig. 7(c) shows the Poincaré projection of the chaotic response. The responses of the deflection \tilde{w} and the velocity $\dot{\tilde{w}}_{,\omega\tau}$ are sampled 6000 points at the phase delay $\theta = 2\pi/3$ radian from the maximum amplitude of the excitation acceleration. The Poincaré projections show a figure with an elbow-shaped bend.

Corresponding to the chaotic response C(1,1 : 1/2), analytical results are shown in Fig. 8 at $\omega = 48.0$. In the numerical integrations of the Runge–Kutta–Gill method, time-step increment $\Delta\tau$ is chosen as 1/240 of the

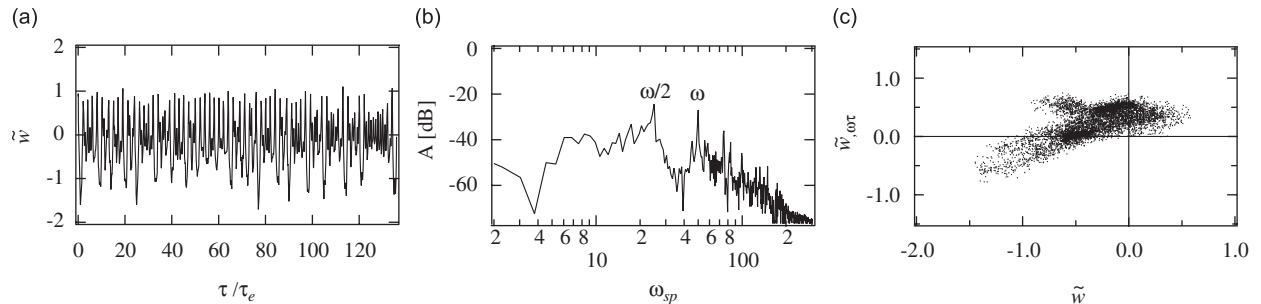


Fig. 7. Chaotic responses C(1,1 : 1/2), experimental results, $\omega = 49.8$: (a) time history; (b) frequency spectrum; (c) Poincaré projection.

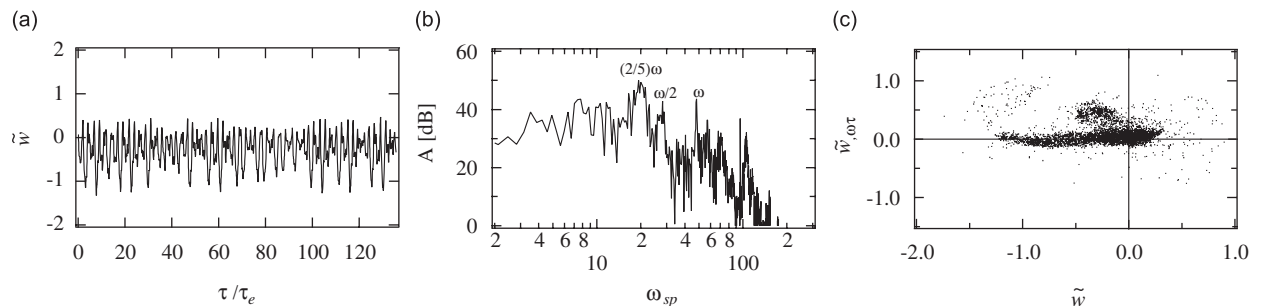


Fig. 8. Chaotic responses C(1,1 : 1/2), analytical results, $\omega = 48.0$: (a) time history; (b) frequency spectrum; (c) Poincaré projection.

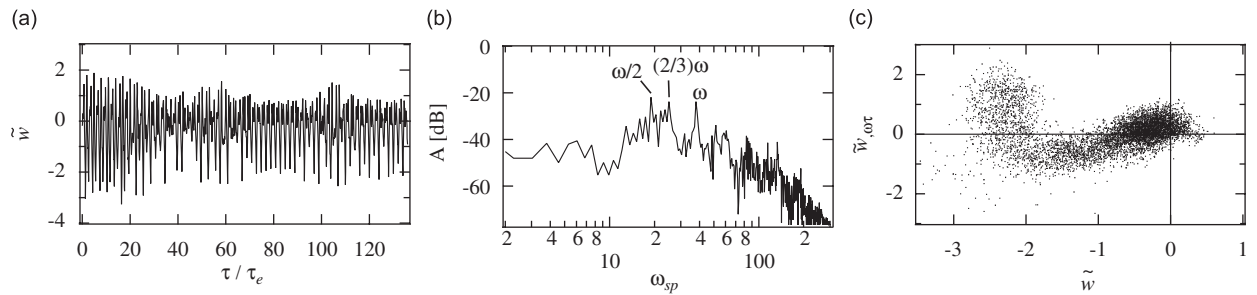


Fig. 9. Chaotic responses $C(1, 1 : 2/3)$, experimental results, $\omega = 38.2$: (a) time history; (b) frequency spectrum; (c) Poincaré projection.

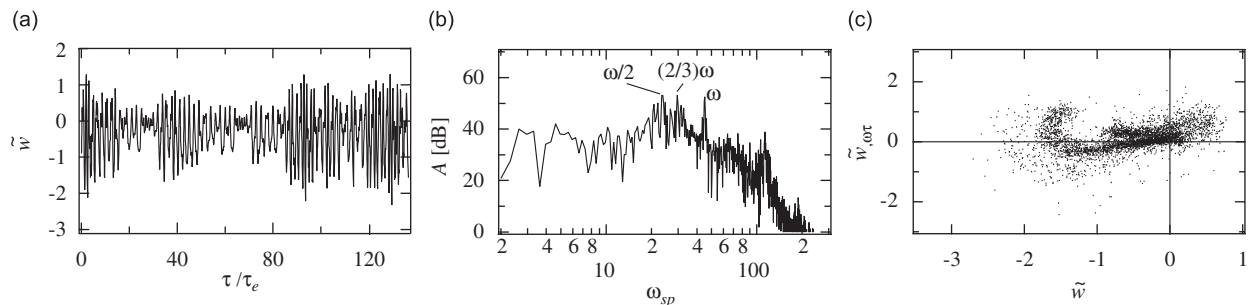


Fig. 10. Chaotic responses $C(1, 1 : 2/3)$, analytical results, $\omega = 45.0$: (a) time history; (b) frequency spectrum; (c) Poincaré projection.

excitation period τ_e . After an initial transient response caused by the numerical integration is well decayed, the response after $3700\tau_e$ is applied for the inspection of chaotic responses. The time history shows the similar movement to the experimental result, even though the peak amplitude is slightly smaller than that of the experiment. The Fourier spectrum of the chaotic response shows the peaks of $(2/5)\omega$ and $\omega/2$ simultaneously. The Poincaré projection has the same aspect as the experimental result.

In Fig. 9, the other chaotic response $C(1, 1 : 2/3)$ in the experiment are detected at the frequency $\omega = 38.2$. The chaotic response is generated in the lower frequency range of the sub-harmonic resonance $(1, 1 : 1/2)$. As shown in Fig. 9(a), the chaotic response $C(1, 1 : 2/3)$ shows the large amplitude response with asymmetric movement with respect to the equilibrium position of $\tilde{w} = 0$. In Fig. 9(b), distinguished spectrum components of the chaotic response clearly appears at the frequencies $(1/2)\omega$ and $(2/3)\omega$ simultaneously. This type of chaotic responses is closely related to the ultra-sub-harmonic resonance of $2/3$ order. The Poincaré projection of the chaos $C(1, 1 : 2/3)$ is shown in Fig. 9(c). The figure of projection curves gently, which is different qualitatively from the figure with an elbow-shaped bend of the chaos $C(1, 1 : 1/2)$ in Fig. 7(c).

In the analysis, predominant chaotic responses $C(1, 1 : 2/3)$ are generated from the excitation frequency $\omega = 44.6$ to 47.8 . Fig. 10 shows the time history, the Fourier spectrum and the Poincaré projection of $C(1, 1 : 2/3)$. In Fig. 10(a) at $\omega = 45.0$, the time history of the chaos shows the large amplitude response. As shown in the frequency–response curves of Fig. 6(b), the amplitude of the chaos overlaps the amplitudes of periodic responses of the sub-harmonic resonance $(1, 1 : 1/2)$ and the ultra-sub-harmonic resonance $(1, 1 : 2/3)$.

In the Fourier spectrum of the chaotic time response in Fig. 10(b), main spikes of the spectrum can be observed related to the resonance responses of the sub-harmonic resonance of $1/2$ order and the ultra-sub-harmonic resonance of $2/3$ order. Comparing the analytical result of the Poincaré projection in Fig. 10(c) with the experimental result in Fig. 9(c), the figures of projections have similar features.

5.4. The maximum Lyapunov exponents and the Lyapunov dimension of the shell-panel

Following the procedure by Wolf et al. [37], our programming code is established. The maximum Lyapunov exponents of the chaotic response of the shell-panel are calculated. If the maximum Lyapunov exponent of

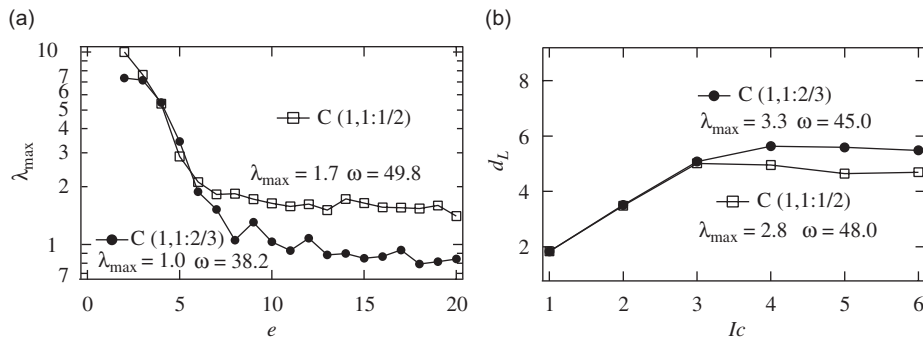


Fig. 11. Maximum Lyapunov exponents and Lyapunov dimension: (a) experimental results of maximum Lyapunov exponent—● $\omega = 38.2$ C(1,1 : 2/3), □ $\omega = 49.8$ C(1,1 : 1/2); (b) analytical results of Lyapunov dimension—● $\omega = 45.0$ C(1,1 : 2/3), □ $\omega = 48.0$ C(1,1 : 1/2).

a response has a positive value the responses can be confirmed as the chaos. Furthermore, increasing the embedding dimension constructed from the chaotic time history, number of vibration modes which contributes to the chaos can be estimated by the convergence of the maximum Lyapunov exponent.

Fig. 11(a) shows the maximum Lyapunov exponents λ_{\max} related to the embedding dimension e in the chaotic responses of C(1,1 : 1/2) and C(1,1 : 2/3) obtained by the experiment. For the chaos C(1,1 : 1/2) as the embedding dimension increases more than $e = 6$, the maximum Lyapunov exponents λ_{\max} converge to a positive constant value $\lambda_{\max} = 1.7$. Half of the embedding dimension corresponds to the number of vibration modes which contributes to the chaos [40]. For the chaotic response C(1,1 : 2/3), the maximum Lyapunov exponent converges to $\lambda_{\max} = 1.0$ as the embedding dimension increases more than $e = 8$ in Fig. 11(a). Consequently, the number of vibration modes in the chaos C(1,1 : 1/2) and C(1,1 : 2/3) are counted as 3 and 4, respectively.

In the analysis, the Lyapunov dimension d_L of the chaotic responses C(1,1 : 1/2) and C(1,1 : 2/3) are calculated by increasing the assumed number of vibration modes I_c . The convergence of the Lyapunov dimensions are shown in Fig. 11(b). When the number of modes I_c in the C(1,1 : 1/2) increases to $I_c = 3$, the value of d_L converges to the value $d_L = 4.8$. The corresponding maximum Lyapunov exponent takes $\lambda_{\max} = 2.8$. For the chaos C(1,1 : 2/3) as the number of mode increases $I_c = 4$, the converged Lyapunov dimension is $d_L = 5.5$ and the maximum Lyapunov exponent is $\lambda_{\max} = 3.3$. The number of vibration modes, contributes to the chaos, has excellent agreement both in the experiment and in the analysis. The maximum Lyapunov exponents have same order. There is still discrepancy between the experimental and analytical results which remain to a future work on the shell-panel.

5.5. Modal interaction in the chaotic responses

By applying the principal component analysis to the chaotic time histories at multiple positions of the shell surface, contributions of vibration modes to the chaotic responses are determined. The chaotic time histories of deflection are measured simultaneously at six positions on the shell surface. The positions are selected as $(\xi = 0.21, \eta = 0.21)$, $(0.5, 0.21)$, $(0.79, 0.21)$, $(0.5, 0.5)$, $(0.79, 0.5)$ and $(0.79, 0.79)$. The measuring positions are arranged on the half-area of the shell surface to detect symmetric and asymmetric modes of vibration.

Using the principal component analysis, contribution ratio and related modal pattern are calculated. Fig. 12(a) shows the contribution ratio and the corresponding modal pattern for the chaotic response C(1,1 : 1/2) at $\omega = 49.8$. The largest principal component, which corresponding to the lowest vibration modes (1,1) prevails contribution ratio of 97 percent. The second larger contribution of 1.6 percent corresponds to the mode with a nodal circle, because modes (1,3) and (3,1) are simultaneously generated. Two modes of same kind with different angular orientation can be combined when the modes are degenerate, i.e., the modes have approximately equal frequencies. These combined modes can be easily generated because the shell-panel has the square boundary with all edges simply supported and the very shallow curvatures. The third contribution of 1.1 percent is related to the combined mode of (1,2) and (2,1), i.e., the mode has one nodal diagonal line.

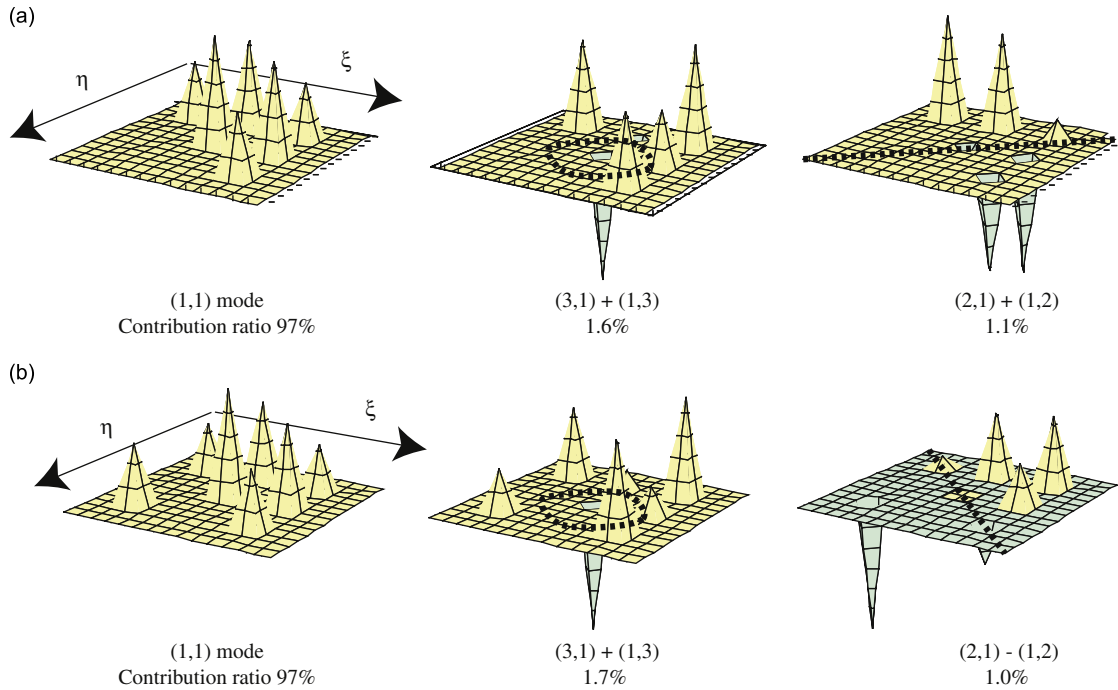


Fig. 12. Modal pattern of principal components, $C(1,1 : 1/2)$: (a) experimental results, $\omega = 49.8$; (b) analytical results, $\omega = 48.0$.

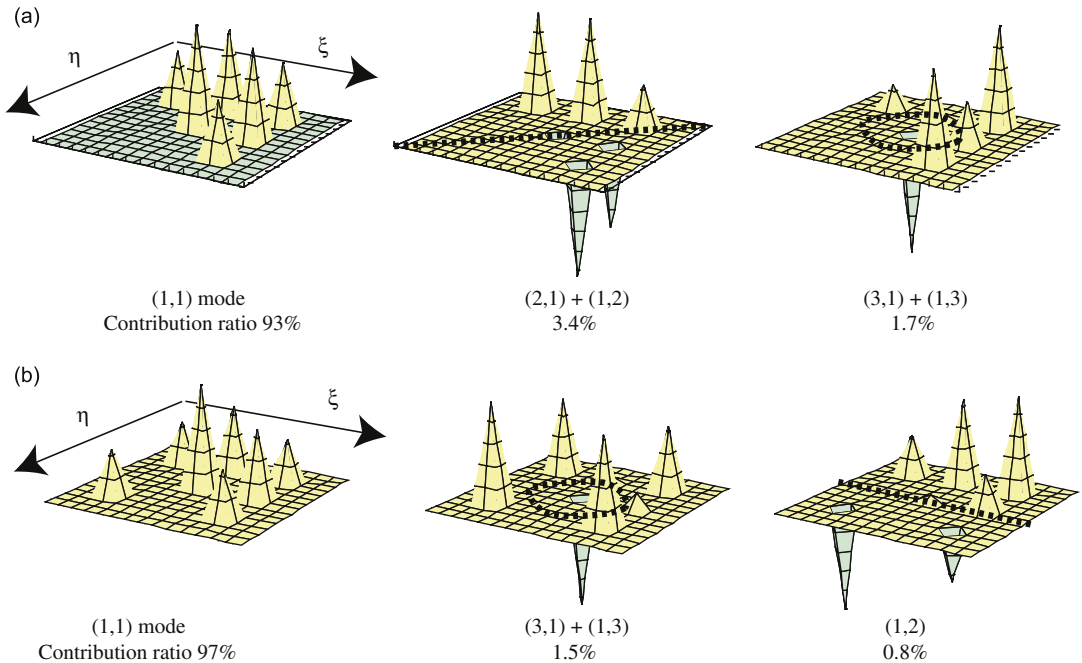


Fig. 13. Modal pattern of principal components, $C(1,1 : 2/3)$: (a) experimental results, $\omega = 38.2$; (b) analytical results, $\omega = 45.0$.

The fourth larger component has 0.5 percent of the higher mode. In the analysis, as shown in Fig. 12(b), the largest contribution ratio is 97 percent of the mode (1,1), while the second larger and the third larger contribution ratios are 1.7 and 1.0 percent, respectively, corresponding to same type of vibration mode of the experiment. The fourth component has 0.3 percent of contribution.

Figs. 13(a) and (b) show the results of principal component analysis in the chaotic response (1,1:2/3) of the experiment and of the analysis, respectively. In Fig. 13(a), the largest component with the vibration mode (1,1) takes 94 percent of contribution, while the second larger contribution takes 3.4 percent with the combined mode of (2,1) and (1,2). The third contribution has 1.7 percent with the combined mode of (3,1) and (1,3). The fourth contribution has 0.9 percent in the higher mode. As shown in Fig. 13(b) of the analytical results, the largest component of the mode (1,1) takes 97 percent. The second component takes 1.5 percent of which mode is the combined mode of (3,1) and (1,3). The third component has 0.8 percent with the combined mode of (2,1) and (1,2). The second and the third components are exchanged in the modal pattern compared with the experimental result. The fourth component has 0.3 percent of contribution. It seems that the exchange of the higher modes comes from the assumption of symmetric configuration of the shell-panel used in the analysis. For the chaotic response of the ultra-sub-harmonic resonance C(1,1 : 2/3) in the experiment, the higher modes of vibration have larger contribution to the chaos compared with the result related to the sub-harmonic resonance C(1,1 : 1/2).

6. Conclusions

Precise experiment and analysis have been carried out on modal interaction in chaotic vibrations of a shallow double-curved shell-panel with simply supported edges subjected to the gravity and periodic acceleration. Main results are summarized as follows.

- (1) The dominant chaotic responses of the shallow shell-panel are generated from the periodic responses of the sub-harmonic resonance of 1/2 order and of the ultra-sub-harmonic resonance of 2/3 order, corresponding to the lowest mode of vibration predominantly.
- (2) The number of vibration modes, which contributes to the chaotic response of the sub-harmonic resonance of 1/2 order, is 3, while the number of vibration modes generated in the chaotic response of the ultra-sub-harmonic resonance of 2/3 order is 4.
- (3) In the chaotic response of the sub-harmonic resonance of 1/2 order, the lowest mode of vibration contributes predominantly. Higher two combined modes, of degenerate vibration modes, with a nodal circle and with a nodal diagonal line have the contribution ratio 2 and 1 percent, respectively. In the chaotic response of the ultra-sub-harmonic resonance of 2/3 order in the experiment, the lowest mode of vibration has a main contribution. The higher three modes of vibration have the contribution ratio from 1 to 3 percent.
- (4) Fairly good agreements are obtained between the experimental results and the analytical results of the chaotic responses.

Acknowledgment

The authors thank Mr. Dai Yanagisawa (Mitsuba Corporation) for his assistance in the fabrication of the shell-panel.

Appendix

The solution of the compatibility equation (1) is expressed as

$$\begin{aligned}
 f = & (1/2)p_y \xi^2 + (1/2)p_x \eta^2 + p_{xy} \xi \eta + \sum_m \sum_n d_{mn}^{(0)} (\hat{b}_{mn} - \hat{a}_{mn}) \sin \bar{m} \xi \sin \bar{n} \eta \\
 & + \sum_k \sum_l \sum_m \sum_n (\hat{b}_{kl} \hat{b}_{mn} - \hat{a}_{kl} \hat{a}_{mn}) \{ \theta_{klmn}^{(1)} \cos(\bar{k} - \bar{m}) \xi \cos(\bar{l} - \bar{n}) \eta \\
 & + \theta_{klmn}^{(2)} \cos(\bar{k} - \bar{m}) \xi \cos(\bar{l} + \bar{n}) \eta + \theta_{klmn}^{(3)} \cos(\bar{k} + \bar{m}) \xi \cos(\bar{l} - \bar{n}) \eta \\
 & + \theta_{klmn}^{(4)} \cos(\bar{k} + \bar{m}) \xi \cos(\bar{l} + \bar{n}) \eta \}, \quad (k, l, m, n = 1, 2, 3, \dots), \tag{17}
 \end{aligned}$$

where notation $\bar{m} = m\pi$ is introduced and $d_{mn}^{(0)}, \theta_{klmn}^{(i)}$ ($i = 1, 2, 3, 4$) are

$$\begin{aligned} d_{mn}^{(0)} &= c(\alpha_y \bar{m}^2 + \alpha_x \beta^2 \bar{n}^2) / (\bar{m}^2 + \beta^2 \bar{n}^2)^2, \\ \theta_{klmn}^{(1)} &= -(c\beta^2/8)(\bar{m}\bar{l} - \bar{k}\bar{n})^2(1 - \delta_{km})(1 - \delta_{ln}) / \{(\bar{k} - \bar{m})^2 + \beta^2(\bar{l} - \bar{n})^2\}^2, \\ \theta_{klmn}^{(2)} &= (c\beta^2/8)(\bar{m}\bar{l} + \bar{k}\bar{n})^2 / \{(\bar{k} - \bar{m})^2 + \beta^2(\bar{l} + \bar{n})^2\}^2, \\ \theta_{klmn}^{(3)} &= (c\beta^2/8)(\bar{m}\bar{l} + \bar{k}\bar{n})^2 / \{(\bar{k} + \bar{m})^2 + \beta^2(\bar{l} - \bar{n})^2\}^2, \\ \theta_{klmn}^{(4)} &= -(c\beta^2/8)(\bar{m}\bar{l} - \bar{k}\bar{n})^2 / \{(\bar{k} + \bar{m})^2 + \beta^2(\bar{l} + \bar{n})^2\}^2. \end{aligned} \quad (18)$$

In the foregoing, the symbol δ_{km} is Kronecker's delta. The arbitrary time functions p_x, p_y and p_{xy} for the in-plane boundary condition of Eq. (7) can be expressed as

$$\begin{aligned} p_y &= \sum_m \sum_n \{d_{mn}^{(1)}(\hat{b}_{mn} - \hat{a}_{mn}) + e_{mn}^{(1)}(\hat{b}_{mn}^2 - \hat{a}_{mn}^2)\} + g_1, \\ p_x &= \sum_m \sum_n \{d_{mn}^{(2)}(\hat{b}_{mn} - \hat{a}_{mn}) + e_{mn}^{(2)}(\hat{b}_{mn}^2 - \hat{a}_{mn}^2)\} + g_2, \\ p_{xy} &= 0, \end{aligned} \quad (19)$$

where $d_{mn}^{(i)}, e_{mn}^{(i)}$ and g_i ($i = 1, 2$) are functions related to the shell geometry, the in-plane spring stiffness and the initial in-plane displacements, respectively.

References

- [1] D.A. Evensen, Some observations on the non-linear vibration of thin cylindrical shells, *American Institute of Aeronautics and Astronautics Journal* 1 (1963) 2857–2858.
- [2] M.D. Olson, Some experimental observations on the nonlinear vibration of cylindrical shells, *American Institute of Aeronautics and Astronautics Journal* 3 (1965) 1775–1777.
- [3] D.A. Evensen, Nonlinear flexural vibrations of thin circular rings, *Transaction of the ASME Series E, Journal of Applied Mechanics* 33 (1966) 553–560.
- [4] Y. Matsuzaki, S. Kobayashi, A theoretical and experimental study on the nonlinear flexural vibration of thin circular cylindrical shell with clamped ends, *Transaction of the Japanese Society for Aeronautics and Space Sciences* 12 (1969) 55–62.
- [5] J.C. Chen, C.D. Babcock, Nonlinear vibration of cylindrical shells, *American Institute of Aeronautics and Astronautics Journal* 13 (1975) 868–876.
- [6] M. Chiba, Non-linear hydroelastic vibration of a cantilever cylindrical tank—I: experiment (empty case), *International Journal of Non-Linear Mechanics* 28 (1993) 591–599.
- [7] F. Pellicano, M. Amabili, M.P. Païdoussis, Effect of the geometry on the non-linear vibration of circular cylindrical shells, *International Journal of Non-Linear Mechanics* 37 (2002) 1181–1198.
- [8] M. Amabili, Theory and experiments for large-amplitude vibrations of empty and fluid-filled circular cylindrical shells with imperfections, *Journal of Sound and Vibration* 262 (2003) 921–975.
- [9] Y. Kobayashi, A.W. Leissa, Large amplitude free vibration of thick shallow shells supported by shear diaphragms, *International Journal of Non-Linear Mechanics* 30 (1995) 57–66.
- [10] M. Amabili, M. Pellegrini, M. Tommesani, Experiment on large-amplitude vibration of a circular cylindrical panel, *Journal of Sound and Vibration* 260 (2003) 537–547.
- [11] E.H. Dowell, Flutter of a buckled plate as an example of chaotic motion of a deterministic autonomous systems, *Journal of Sound and Vibration* 85 (1982) 333–344.
- [12] A.H. Nayfeh, R.A. Raouf, Nonlinear forced response of infinitely long circular shells, *Journal of Applied Mechanics* 54 (1987) 571–577.
- [13] H.L. Yang, P.R. Sethna, Non-linear phenomena in forced vibrations of a nearly square plate, *Journal of Sound and Vibration* 155 (1992) 413–441.
- [14] S.I. Chang, A.K. Bajaj, C.M. Krousgrill, Nonlinear vibrations and chaos in harmonically excited rectangular plates with one-to-one internal resonance, *Nonlinear Dynamics* 4 (1993) 433–460.
- [15] J. Fan, F. He, Z. Liu, Chaotic oscillation of saddle form cable-suspended roofs under vertical excitation action, *Nonlinear Dynamics* 12 (1997) 57–68.
- [16] M.S. Soliman, P.B. Gonçalves, Chaotic behavior resulting in transient and steady state instabilities of pressure-loaded shallow spherical shells, *Journal of Sound and Vibration* 259 (2003) 497–512.
- [17] M. Amabili, Non-linear vibrations of doubly curved shallow shells, *International Journal of Non-Linear Mechanics* 40 (2005) 683–710.
- [18] R.C. Zhou, D.Y. Xue, C. Mei, Finite element time domain-modal formulation for nonlinear flutter of composite panels, *American Institute of Aeronautics and Astronautics Journal* 32 (1994) 2042–2052.

- [19] C. Sansour, P. Wriggers, J. Sansour, Nonlinear dynamics of shells: theory, finite element formulation, and integration schemes, *Nonlinear Dynamics* 13 (1997) 279–305.
- [20] L. Maestrello, A. Frendi, D.E. Brown, Nonlinear vibration and radiation from a panel with transition to chaos, *American Institute of Aeronautics and Astronautics Journal* 30 (1992) 2632–2638.
- [21] K.D. Murphy, L.N. Virgin, S.A. Rizzi, Characterizing the dynamics response of a thermally loaded, acoustically excited plate, *Journal of Sound and Vibration* 196 (1996) 635–658.
- [22] K. Nagai, Nonlinear vibrations of a shallow arch under periodic lateral force (Theory), *Transaction of the Japan Society of Mechanical Engineers* 51 (1985) 2820–2827 (in Japanese).
- [23] K. Nagai, Nonlinear vibrations of a shallow arch under periodic lateral force (2nd Report, Experiment), *Transaction of the Japan Society of Mechanical Engineers* 52 (1986) 3047–3054 (in Japanese).
- [24] K. Nagai, Experimental study of chaotic vibration of a clamped beam subjected to periodic lateral forces, *Transaction of the Japan Society of Mechanical Engineers* 56 (1990) 1171–1177 (in Japanese).
- [25] K. Nagai, T. Yamaguchi, Chaotic vibrations of a post-buckled beam carrying a concentrated mass (1st Report, Experiment), *Transaction of the Japan Society of Mechanical Engineers* 60 (1994) 3733–3740 (in Japanese).
- [26] T. Yamaguchi, K. Nagai, Chaotic vibrations of a post-buckled beam carrying a concentrated mass (2nd Report, Theoretical Analysis), *Transaction of the Japan Society of Mechanical Engineers* 60 (1994) 3741–3748 (in Japanese).
- [27] K. Nagai, K. Kasuga, M. Kamada, T. Yamaguchi, K. Tanifuji, Experiment on chaotic oscillations of a post-buckled reinforced beam constrained by an axial spring, *International Journal of the Japan Society of Mechanical Engineers* 41 (1998) 563–569.
- [28] K. Nagai, S. Maruyama, K. Sakaimoto, T. Yamaguchi, Experiments on chaotic vibrations of a post-buckled beam with an axial elastic constraint, *Journal of Sound and Vibration* 304 (2007) 541–555.
- [29] K. Nagai, T. Yamaguchi, Chaotic oscillations of a shallow cylindrical shell with rectangular boundary under cyclic excitation, *High Pressure Technology, ASME, PVP* 297 (1995) 107–115.
- [30] T. Yamaguchi, K. Nagai, Chaotic vibration of a cylindrical shell-panel with an in-plane elastic-support at boundary, *Nonlinear Dynamics* 13 (1997) 259–277.
- [31] K. Nagai, S. Maruyama, M. Oya, T. Yamaguchi, Chaotic oscillations of a shallow cylindrical shell with a concentrated mass under periodic excitation, *Computers and Structures* 82 (2004) 2607–2619.
- [32] K. Nagai, S. Maruyama, T. Murata, T. Yamaguchi, Experiments and analysis on chaotic vibrations of a shallow cylindrical shell-panel, *Journal of Sound and Vibration* 305 (2007) 492–520.
- [33] B.F. Feeny, R. Kappagantu, On the physical interpretation of proper orthogonal modes in vibrations, *Journal of Sound and Vibration* 211 (4) (1998) 607–616.
- [34] L.H. Donnell, Stability of thin-walled tubes under torsion, *NACA Report* 479 (1935) 95–116.
- [35] C.S. Ventres, E.H. Dowell, Comparison of theory and experiment for nonlinear flutter of loaded plates, *American Institute of Aeronautics and Astronautics Journal* 8 (1970) 2022–2030.
- [36] M. Urabe, A. Reiter, Numerical computation of nonlinear forced oscillations by Galerkin's procedure, *Journal of Mathematical Analysis and Applications* 14 (1966) 107–140.
- [37] A. Wolf, J.B. Swift, H.L. Swinney, J.A. Vastano, Determining Lyapunov exponents from a time series, *Physica D* 16 (1985) 285–317.
- [38] F. Takens, Detecting strange attractors in turbulence, in: D. Rand, L. Young (Eds.), *Lecture Notes in Mathematics*, Vol. 898, Springer, New York, 1981, pp. 366–381.
- [39] J. Kaplan, J. Yorke, The Lyapunov dimension of strange attractors, *Journal of Differential Equations* 49 (1983) 185–207.
- [40] C. Pezeshki, E.H. Dowell, Generation and analysis of Lyapunov exponents for the buckled beam, *International Journal of Non-Linear Mechanics* 24 (2) (1989) 79–97.
- [41] M.M. Loève, *Probability Theory*, Van Nostrand, Princeton, NJ, 1955.